

Interventional Heart Wall Motion Analysis with Cardiac C-arm CT Systems

Kerstin Müller^{1,2}, Andreas K. Maier^{1,2}, Yefeng Zheng³,
Yang Wang³, Günter Lauritsch⁴, Chris Schwemmer^{1,2},
Christopher Rohkohl⁴, Joachim Hornegger^{1,2} and Rebecca
Fahrig⁵

¹Pattern Recognition Lab, Department of Computer Science,
Friedrich-Alexander-Universität Erlangen-Nürnberg, Martensstr. 3, D-91058
Erlangen, Germany

²Erlangen Graduate School in Advanced Optical Technologies (SAOT),
Paul-Gordan-Str. 6, D-91052 Erlangen, Germany

³Imaging and Computer Vision, Siemens Corporate Research, 755 College Road
East, Princeton, NJ-08540, USA

⁴Siemens AG, Healthcare Sector, Siemensstr. 1, D-91301 Forchheim, Germany

⁵Department of Radiology, Stanford University, 1201 Welch Road, Stanford
CA-94305, USA

E-mail: kerstin.mueller@cs.fau.de

Abstract. Today, quantitative analysis of 3-D dynamics of the left ventricle (LV) cannot be performed directly in the catheter lab using a current angiographic C-arm system, which is the workhorse imaging modality for cardiac interventions. Therefore, myocardial wall analysis is completely based on the 2-D angiographic images or pre-interventional 3-D/4-D imaging. In this paper, we present a complete framework to study the ventricular wall motion in 4-D (3-D+ t) directly in the catheter lab. From the acquired 2-D projection images, a dynamic 3-D surface model of the LV is generated, which is then used to detect ventricular dyssynchrony. Different quantitative features to evaluate LV dynamics known from other modalities (ultrasound, MR) are transferred to the C-arm CT data. We use the ejection fraction (EF), the systolic dyssynchrony index (SDI), a 3-D fractional shortening (3DFS _{i}) and the phase to maximal contraction ($\phi_{i,\max}$) to determine an indicator of LV dyssynchrony and to discriminate regionally pathological from normal myocardium. The proposed analysis tool was evaluated on simulated phantom LV data with and without pathological wall dysfunctions. The used LV data is publicly available online at <https://conrad.stanford.edu/data/heart>. In addition, the presented framework was tested on eight clinical patient data sets. The first clinical results demonstrate promising performance of the proposed analysis tool and encourage the application of the presented framework to a larger study in clinical practice.

1. Introduction

Today, interventional cardiac imaging is based on angiographic C-arm systems. However, to date no quantitative 3-D/4-D analysis of the left ventricle (LV) has been performed during the intervention using angiographic C-arm CT. Functional imaging is usually performed pre-interventionally by other devices, mainly ultrasound (US) (Kapetanakis et al. 2005, Jenkins et al. 2004), magnetic resonance imaging (MRI) (Matthew et al. 2012, Ma et al. 2012) or cardiac computed tomography angiography (CCTA) (Lee et al. 2012, Po et al. 2011). The CCTA and MRI have to be performed before the cardiac intervention. The three-dimensional echocardiographic images are also acquired before the intervention, since it interrupts the clinical workflow of the cardiac procedure. Our goal is a one-step solution of functional cardiac imaging within the catheter lab using the interventional C-arm system. In an interventional set-up, C-arm systems are the main modality used for performing cardiac interventions under fluoroscopic imaging. In addition, the same systems can be used to generate CT images of the heart (Lauritsch et al. 2006). The major challenge to providing 3-D cardiac images and hence functional parameters in the interventional suite is the low temporal resolution of the C-arm system which limits the 3-D visualization of the moving heart based on conventional reconstruction algorithms. Considerable progress has been made in the field of motion-compensated tomographic reconstructions of the heart chambers from C-arm CT data (Prümmer et al. 2009, Isola et al. 2010, Müller, Zheng, Wang, Lauritsch, Rohkohl, Schwemmer, Maier, Schultz, Hornegger & Fahrig 2013). These approaches provide several motion-compensated reconstructions of different heart phases and hence 4-D (3-D+ t) images of the heart.

A combination of the motion-compensated reconstruction with a quantitative analysis of the dynamics of the left heart ventricle (LV) would provide valuable diagnostic information. From the dynamic 3-D US images different parameters are extracted to analyse LV synchrony. The systolic dyssynchrony index (SDI), as defined in Kapetanakis et al. (Kapetanakis et al. 2005), is based on the analysis of the time passed to reach the minimal volume for specific LV regions as percentage of the cardiac cycle. The standard deviation of these timings defines the SDI. In Herz et al. (Herz et al. 2005), the quantitative wall motion analysis is based on a finite element model of the LV and the dynamics are studied using a three-dimensional fractional shortening (3DFS), which is a generalisation of the fractional shortening from 2-D US (Moynihan et al. 1981). Recently, an approach to detect LV dyssynchrony in cardiac computed tomography angiography (CCTA) was proposed by Po et al. (Po et al. 2011). They utilize the same model as in Herz et al. and differentiate synchronous from dyssynchronous LVs by the time elapsed before each model point reaches its maximal contraction point. If the LV contracts synchronously, the time to maximal contraction is homogeneous over the LV. If not, regional wall motion abnormalities can be detected. The extracted LV motion information could improve the outcome of complex cardiac procedures, such as cardiac resynchronization therapy (CRT). The LV model can guide a physician to an optimal position of the LV lead and hence, increase the rate of success of these interventions (Ma et al. 2012).

In the literature, several approaches to recover the 3-D shape of the left ventricle with biplane X-ray systems are described. When using a biplane system, the epipolar constraint can be exploited in order to compute the 3-D LV shape from two orthogonal simultaneously acquired projection images (Hartley & Zisserman 2004). In Backfrieder et al. (Backfrieder et al. 2005), initial super ellipses are deformed until their projection

profiles optimally fit to the measured projections. The generated model can be used to perform an LV wall motion analysis (Swoboda et al. 2005). The results were promising, but no quantitative analysis was performed. A similar approach is used in Medina et al. and Mantilla et al. (Medina et al. 2006, Mantilla et al. 2008), where ellipsoidal approximations derived from the input ventriculograms are deformed to match the input projections. The mentioned approaches differ in the representation of the LV geometry and their optimization procedure. Other approaches also make use of multi-view cardiograms. Moriyama et al. (Moriyama et al. 2002) proposed an iterative framework to recover LV meshes from multi views by fitting a 4-D surface model defined by B-splines to the LV. All of the mentioned approaches make use of the synchronously acquired orthogonal ventriculograms from a biplane system. Most of the presented work utilizes ellipsoidal structures for the reconstruction of the LV. More degrees of freedom for the surface generation can improve the reconstruction of the dynamic LV surface.

In this paper, we present a complete framework towards an automatic interventional wall motion analysis tool to study LV dynamics in 4-D (3-D+ t). This approach would provide a one-step solution without the need to switch to another modality during the intervention. The previously described parameters are adapted to dynamic C-arm CT in order to provide a quantitative 4-D analysis of the LV.

2. Dynamic Left Ventricle Imaging and Analysis

The individual steps required to compute a dynamic surface model of the LV are: 1) the image acquisition of the LV 2) fitting an initial mesh to the standard FDK reconstruction (Feldkamp et al. 1984) using all projection images 3) segmentation of the 2-D bloodpool 4) heart phase identification 5) adaptation of the surface mesh 6) left ventricle representation and 7) motion analysis. The individual steps are explained in more detail in the following subsections.

2.1. Image Acquisition

The image acquisition protocol for an LV scan with a C-arm system consists of a few hundred projection images (≈ 200 – 300) over an angular range of 200° in 5 s–10 s during a breath hold. A contrast agent is administered directly into the LV at 10 ml/s by a pigtail catheter inserted via the femoral artery in the leg or radial/brachial artery in the arm. Imaging starts with a delay of ~ 1 s, the time needed for the contrast to fill the LV homogeneously. Detailed acquisition parameters used in the experiments are given in Section 3.

2.2. Initial Surface Mesh

An initial 3-D mesh is generated from the standard FDK reconstruction (Feldkamp et al. 1984) using all projection images. This reconstruction still exhibits artefacts due to cardiac motion, but the reconstruction quality is sufficient for extraction of a static and preliminary 3-D LV endocardium mesh using a marginal space learning and steerable feature approach proposed by Zheng et al. (Zheng et al. 2008).

2.3. 2-D Bloodpool Segmentation

For the heart phase identification and the generation of the dynamic surface model, the 2-D segmented bloodpool of the LV is required. The bloodpool segmentation is based on a boundary defined by a set of connected points. For each of these points, the steerable features (Zheng et al. 2008) centred at this point location are extracted to train a probabilistic boosting tree (PBT) classifier (Tu 2005). During the training stage, the manually annotated LV bloodpool boundary is given as the input to extract positive samples (on the true boundary) and negative samples (far away from the boundary). During testing, the features along the normal direction of the initial 2-D forward projected static mesh are extracted as the input to the trained classifier, and the candidate location with the peak probability score is selected as detected contour location (Chen et al. 2011).

2.4. Heart Phase Identification

The heart phase $\phi(t) \in [0\%, \dots, 100\%]$ of each projection at acquisition time t needs to be identified. For patients with an irregular heart rhythm the cardiac phase cannot be assigned from the electrocardiogram (ECG) signal by linear interpolation between two R-R peaks in the same manner as with a regular heart beat (Lauritsch et al. 2006). Therefore, the 2-D segmented bloodpool area is used for identification of the heart phase. The 2-D bloodpool size $\pi(t) \in \mathbb{Z}$ at acquisition time t , given as the segmented area in pixels in the 2-D projection images, is filtered with a 1-D Gaussian kernel in order to obtain a smoothed bloodpool curve $\pi_f(t)$, c.f. Figure 1a. The minimum and maximum points are then identified as candidate points for end-systole (ES) t_{ES} and end-diastole (ED) t_{ED} (marked as green and red circles in Figure 1a). A pre-defined threshold is used to exclude false local maxima and minima (c.f. Figure 1a, frames 102 and 110, red and green rings). The detected ED's divide the signal $\pi_f(t)$ into multiple cardiac cycles. In order to generate a reference time-size curve $\bar{\pi}(\xi)$, an intermediate heart phase $\xi \in [0\%, \dots, 100\%]$ is introduced

$$\xi = \frac{t - t_{ED1}}{t_{ED2} - t_{ED1}}, \quad (1)$$

where t_{ED1} and t_{ED2} are the first and last ED points of the current cycle. The bloodpool curve of each cycle is temporally re-sampled to fit to an average length of a cardiac cycle. The re-sampled curves are then averaged over all cycles to generate $\bar{\pi}(\xi)$. An example of a reference curve $\bar{\pi}(\xi)$ is shown in Figure 1b. In order to eliminate the size variation of the bloodpool due to the rotation of the C-arm system, a normalized bloodpool size $\pi_n(t)$ is computed as follows:

$$\pi_n(t) = \begin{cases} \frac{\pi_f(t) - \pi_f(t_{ES})}{\pi_f(t_{ED1}) - \pi_f(t_{ES})} \cdot (\bar{\pi}(0) - \bar{\pi}(\xi_{ES})) + \bar{\pi}(\xi_{ES}), & t < t_{ES} \\ \frac{\pi_f(t) - \pi_f(t_{ES})}{\pi_f(t_{ED2}) - \pi_f(t_{ES})} \cdot (\bar{\pi}(1) - \bar{\pi}(\xi_{ES})) + \bar{\pi}(\xi_{ES}), & t \geq t_{ES} \end{cases} \quad (2)$$

where ξ_{ES} is the ES time point of the reference curve $\bar{\pi}(\xi)$, with

$$\xi_{ES} = \arg \min_{\xi} \bar{\pi}(\xi) \quad (3)$$

and t_{ES} is the end-systolic point of the cardiac cycle containing the currently considered frame. Finally, the cardiac phase $\phi(t)$ for each projection and time point can be obtained based on a quasi-inverse mapping of $\bar{\pi}(\xi)$ at the systolic and diastolic period separately,

$$\phi(t) = \bar{\pi}^{-1}(\pi_n(t)), \quad (4)$$

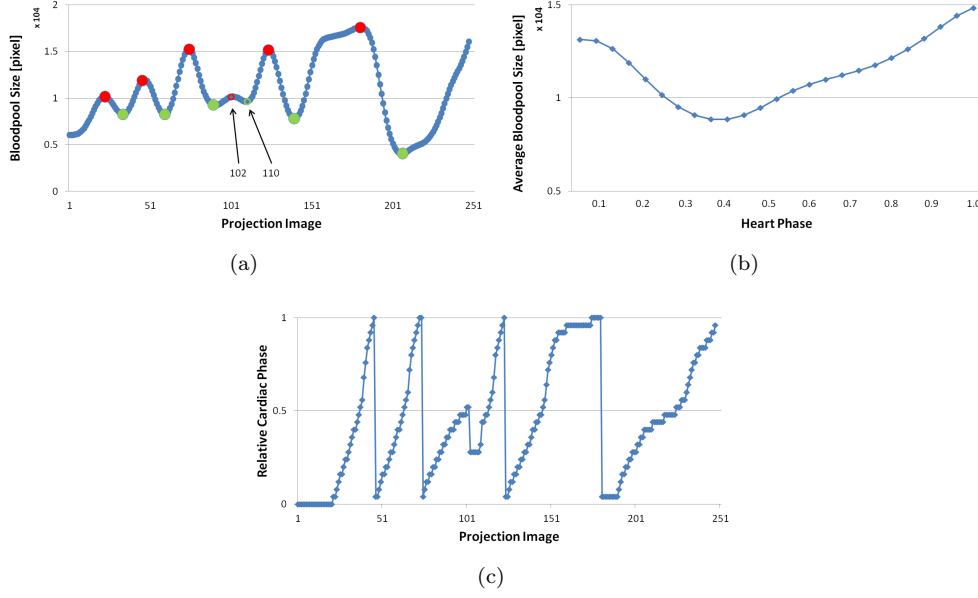


Figure 1: Examples of (a) a smoothed bloodpool segmentation size $\pi_f(t)$ and (b) the mean bloodpool signal $\bar{\pi}(\xi)$ by averaging multiple cardiac cycles. (c) shows the derived cardiac phase $\phi(t)$ based on Equation 4. The candidate end-diastole (ED) time t_{ED} and end-systole (ES) time t_{ES} are marked as red circles and green circles and the red and green ring mark the additional smaller contraction in (a).

where a systolic period is present if $t < t_{ES}$ and a diastolic period otherwise. The continuous heart phase $\phi(t)$ is binned into a number of K heart phases by nearest-neighbour classification and denoted with ϕ_k , with $k = 1, \dots, K$. The number of heart phases K can be chosen according to the number of frames per heart cycle. An example of a derived cardiac phase signal $\phi(t)$ is given in Figure 1c. If a local maximum is detected which is not ED, as illustrated in Figure 1a at frame 102, the phase labelling process based on Equation 4 is reset to the systolic period. At the beginning and end of the scan, if no full cardiac cycle is detected, the local maximum and minimum are used for fitting the half cycle to the average bloodpool signal and the cardiac phase can be assigned as previously described. In the example in Figure 1a no local minimum is detected at the beginning and hence the heart phases at the beginning of the scan are set to zero, see Figure 1c.

2.5. Dynamic Surface Model Generation

A dynamic 3-D surface model of the LV is computed with an initial 3-D mesh which is generated from the standard FDK reconstruction (Feldkamp et al. 1984) using all projection images. The projections are assigned to certain heart phases corresponding to the bloodpool size signal generated from the 2-D projection images described in Subsection 2.4. Then, the initial triangle mesh is dynamically adapted so that the forward projected silhouettes fit to the corresponding LV boundary in the projection images of the same heart phase as proposed by Chen et al. (Chen et al. 2011). As a next step, a 3-D triangulated mesh is generated for every heart phase ϕ_k with its

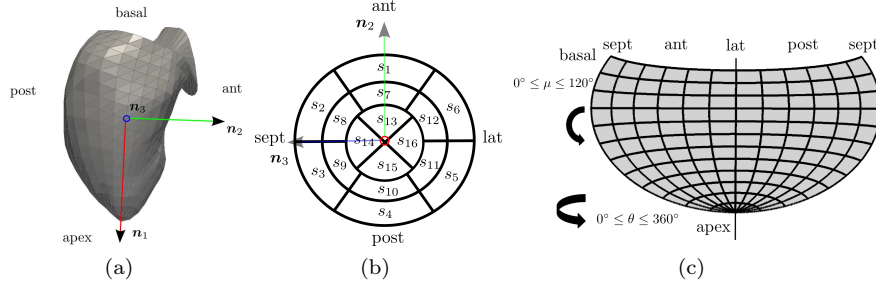


Figure 2: (a) Septal view of one left ventricle surface model at end-diastole with the local coordinate system $(\mathbf{n}_1, \mathbf{n}_2, \mathbf{n}_3)$. \mathbf{n}_3 is pointing towards the reader. (b) Circumferential polar plot of the 16 myocardial segments with the used coordinate system $(\mathbf{n}_1, \mathbf{n}_2, \mathbf{n}_3)$. \mathbf{n}_1 is pointing towards the reader. (c) Hammer projection (Subsection 2.7.3) used to preserve the areas while mapping varying measures of function from 3-D to 2-D.

control points $\mathbf{p}_i(\phi_k) \in \mathbb{R}^3$, with $i = 1, \dots, N$ where N is the number of control points.

2.6. Left Ventricle Representation

In order to analyse the contraction behaviour of the LV, an orthogonal local coordinate system is introduced. The three orthogonal main axes of the end-diastolic LV surface are computed by a modified principal component analysis (PCA) with a rotation and an adjustment of the centroid. The coordinate system is then fixed for the whole analysis. The 1st principal axis $\mathbf{n}_1 \in \mathbb{R}^3$ points towards the long axis of the LV from the middle point of the mitral valve to the apex point. The 2nd axis $\mathbf{n}_2 \in \mathbb{R}^3$, points into the anterior direction and the 3rd axis $\mathbf{n}_3 \in \mathbb{R}^3$ in the septal direction. Initially, \mathbf{n}_1 does not necessarily pass through the apex, since the LV is not necessarily symmetric. Therefore, the coordinate system $(\mathbf{n}_1, \mathbf{n}_2, \mathbf{n}_3)$ is rotated to align \mathbf{n}_1 with the long axis. The origin of the coordinate system is defined as the mid point between base and apex. A schematic of the three coordinate axes is provided in Figure 2a.

The LV surface is divided into 16 segments according to the recommendation of the American Heart Association (AHA) and each point \mathbf{p}_i is assigned to one of these segments (Cerqueira et al. 2002). The 16 myocardial segments are illustrated in Figure 2b.

2.7. Motion Analysis

2.7.1. Volume Computation. For every heart phase the three-dimensional LV volume $\Pi \in \mathbb{R}^+$ is computed. The mapping between the heart phase and each acquisition time point t is known (c.f. Subsection 2.4). The end-diastolic volume (EDV) and end-systolic volume (ESV) are determined as maximum and minimum volume. The ejection fraction (EF) is the difference between the end-diastolic volume and the end-systolic volume compared to the end-diastolic volume. The EF is computed as

$$\text{EF}[\%] = \frac{\text{EDV} - \text{ESV}}{\text{EDV}}. \quad (5)$$

A normal EF has a lower limit of $\sim 50\%$, below that value the contraction ability of the LV is impaired (Pfisterer et al. 1985).

2.7.2. Wall Motion in 3-D. The ventricular wall motion can be analysed in 3-D using different features adapted from other modalities (CCTA, US, MR):

Heart Phase to Maximal Contraction ($\phi_{i,max}$): The minimal Euclidean distance $\lambda_i(\phi_k)$ from every point $\mathbf{p}_i(\phi_k)$ to the long axis \mathbf{n}_1 can be computed. In order to eliminate small outliers, the distance signal for each point is temporally filtered by a 1-D mean filter with a kernel size of 5. Finally, for every surface point, the phase until it reaches its maximum of contraction $\phi_{i,max}$ can be determined. For healthy, synchronous LV motion, a uniform distribution over the entire LV surface can be observed. A higher variability in the contraction times occurs for dyssynchronous dynamics (Po et al. 2011).

Systolic Dyssynchrony Index (SDI): The systolic dyssynchrony index (SDI) known from echocardiography (Gimenes et al. 2008, Kapetanakis et al. 2005, Sachpekidis et al. 2011) can be estimated with the LV volumetric information for every heart phase. For each surface point $\mathbf{p}_i(\phi_k)$ the associated myocardial segment is known at all heart phases. Therefore, the subvolume of each segment can be determined by dividing the LV surface into small triangle pyramids given by the surface mesh and the origin of the coordinate system. In order to eliminate small outliers, the subvolume signals are temporally filtered by a mean filter with a kernel size of 5. For each segment, the phase $\phi_{s,max}$ of maximal contraction and the overall mean phase of maximal contraction ϕ_{max} for all segments are computed. The standard deviation of the maximal contraction phases among the segments is an indicator for LV synchrony

$$SDI = \sqrt{\frac{1}{16} \sum_{s=1}^{16} (\phi_{s,max} - \phi_{max})^2}. \quad (6)$$

Since the SDI represents the standard deviation between contraction phases, a higher SDI denotes increased ventricular dyssynchrony. For echocardiography, Kapetanakis et al. stated an $SDI \leq 3.5 \pm 1.8\%$ as normal, mild disease SDI of $5.4 \pm 0.8\%$, moderate disease SDI of $10.0 \pm 2\%$ and a severe disease SDI of $15.6 \pm 1\%$ (Kapetanakis et al. 2005). It should be mentioned that the SDI is a relatively new parameter of dyssynchrony and it still varies between the methods of measurement (Sachpekidis et al. 2011), but irrespective of the analysis software there is an agreement that healthy individuals rarely have SDI values over 6%.

Three-dimensional Fractional Shortening ($3DFS_i$): In 2-D echocardiography, the fractional shortening of the LV is used as an indicator to identify pathological dynamics. Ischemic regions can be distinguished from normal areas of the LV. Fractional shortening specifies the relationship between the LV radius in diastole and its decrease in systole. Here, a three-dimensional fractional shortening ($3DFS_i$) can be computed similar to (Herz et al. 2005). The $3DFS_i$ value for every point is defined as

$$3DFS_i = \frac{\lambda_{i,ED} - \lambda_{i,ES}}{\lambda_{i,ED}}, \quad (7)$$

where $\lambda_{i,ED}$ and $\lambda_{i,ES}$ denote the Euclidean distance of the mesh point $\mathbf{p}_i(\phi_k)$ to the long axis \mathbf{n}_1 in end-diastole and end-systole, respectively. Herz et al. classified the wall motion as normal ($3DFS_i > 0.25$), hypokinetic ($0.05 < 3DFS_i \leq 0.25$), akinetic ($-0.05 < 3DFS_i \leq 0.05$) or dyskinetic ($3DFS_i \leq -0.05$). The lower limit of normal is based on the standards for 2-D fractional shortening of the American Society of Echocardiography while the values to separate akinesis and dyskinesis are chosen arbitrarily (Herz et al. 2005).

2.7.3. Hammer Projection. In order to provide the point-based indicators in an overview map, a Hammer projection map is created (Hunter & Smaill 1988). The maximal contraction phase $\phi_{i,max}$ and the fractional shortening $3DFS_i$ are mapped from the LV mesh surface to 2-D as a function of location from apex to base ($0^\circ \leq \mu \leq 120^\circ$) and circumferential position ($0^\circ < \theta \leq 360^\circ$). The Hammer projection maps the surface motion information to 2-D while preserving relative surface areas (see also Figure 2c) (Hunter & Smaill 1988). The LV surface is represented by a small number of control points, therefore, the surface with its point-based motion information is re-sampled. The surface is re-sampled with an angular increment of 0.25° in the μ and θ directions. The scalar value at the sample point is computed by simple averaging of the information given at the circumjacent triangle vertices ($\phi_{i,max}$ or $3DFS_i$).

3. Experiments

3.1. Phantom Data

The analysis presented here has been applied to LV surface models generated from a cardiac phantom (Maier et al. 2012, Müller, Maier, Fischer, Bier, Lauritsch, Schwemmer, Fahrig & Hornegger 2013, Maier et al. 2013), which is similarly designed to the widely used 4-D XCAT phantom (Segars et al. 2008). The phantom is defined by cubic B-splines and can be tessellated to generate a triangulated mesh for every time point. The splines can be sampled at any number of points. In our experiments, we sampled the spline at about ≈ 870 surface points. The simulated acquisition protocol uses a total of 133 projection images with a size of 1240×960 pixels and a pixel resolution of 0.3 mm. The dynamic LV surface models were simulated over 5 s at a heart rate of 60 bpm. Five different surface phantoms were generated with various contraction dynamics and considered as ground truth (GT), denoted as $p_{1,GT}$ – $p_{5,GT}$. For the evaluation of the phantom data, dynamic phantom meshes were generated using the initial mesh generation, described in Subsection 2.2. The 2-D segmentation of the phantom data cannot be used to validate the bloodpool segmentation since the segmentation of clinical LV acquisitions and the segmentation of phantom simulations are not comparable. Therefore, the GT 2-D segmentations of the left ventricles were used for the heart phase identification and to generate the dynamic LV meshes (c.f. Subsections 2.4 and 2.5). The meshes had 545 control points uniformly distributed over the left ventricle and are denoted as p_1 – p_5 .

Modelling of Pathological Motion Patterns. For every normalized time point $t \in [0, 1]$ of the whole scan there exists a 2-D spline surface $\mathbf{s} \in [0, 1]^2$. Each spline is defined by control points $\mathbf{c} \in \mathbb{R}^2$ with a one-to-one mapping from 3-D coordinates $\mathbf{C} \in \mathbb{R}^3$ to the 2-D control points \mathbf{c} given by the 4-D XCAT phantom (Segars et al. 1999, Segars et al. 2008). In order to incorporate a motion defect, a region in which the motion

should be pathological has to be defined. Here, a box \mathcal{B} is defined, within the coordinate system of the heart, i.e. a local coordinate system where the z-axis is aligned with the long axis of the LV. Each spline control point \mathbf{C} is clipped against the volume \mathcal{B} , generating a list \mathcal{C}_{path} of control points inside the pathological volume, where the complete set of all control points is denoted as \mathcal{C} . During the tessellation procedure $T(\mathbf{s}, t) : \mathbb{R}^2 \rightarrow \mathbb{R}^3$, the 2-D spline surface points \mathbf{s} are assigned to a 3-D coordinate $\mathbf{x}(t) = T(\mathbf{s}, t)$. In order to allow for a smooth transition between \mathcal{B} and the healthy LV surface, a flexibility parameter σ is introduced. A larger value of σ results in a smooth defect, while a small value yields sharp transitions between pathological and normal tissue. The model incorporates two kinds of motion defects: akinetic wall motion and delayed contraction behaviour. The akinetic motion defect prevents contraction or inward motion of the heart in the affected area. A delayed motion is a contradictory movement of the heart. The motion defects can be controlled by a phase shift parameter $\delta \in [0, 1]$. The deformed 3-D coordinate can then be computed as

$$\mathbf{x}_{path}(t) = (1 - w(\mathbf{s}, t)) \cdot T(\mathbf{s}, t) + w(\mathbf{s}, t) \cdot T(\mathbf{s}, t - \delta), \quad (8)$$

$$w(\mathbf{s}, t) = \frac{\sum_{\mathbf{c} \in \mathcal{C}_{path}} w'(\mathbf{s}, \mathbf{c}, t)}{\sum_{\mathbf{c} \in \mathcal{C}} w'(\mathbf{s}, \mathbf{c}, t)}, \quad (9)$$

$$w'(\mathbf{s}, \mathbf{c}, t) = e^{-\frac{1}{2\sigma^2} \|\mathbf{s} - \mathbf{c}\|_2^2}. \quad (10)$$

The Gaussian basis function $w'(\mathbf{s}, \mathbf{c}, t)$ gives a small weight to control points far away from the current spline surface point \mathbf{s} and a higher weight to close control points. Effectively, $\mathbf{x}_{path}(t)$ is a linear combination between the transformed spline point \mathbf{s} at the current time t and at a time point $t - \delta$. An akinetic motion defect can be realized by setting $\delta = t - t_0$. In our experiments, we set $t_0 = 0$. Hence, the magnitude of the motion in the pathological volume is minimal compared to the motion of the remaining LV. A shift in the motion phase is achieved by setting δ to a fixed value, given as percentage of the heart cycle. Consequently, $\mathbf{x}_{path}(t)$ is generated from the transformed spline points at the current time and at an earlier time with a fixed phase shift. As a result, the motion in the pathological volume is delayed compared to the motion of the remaining LV.

Five different phantom datasets were simulated. The LV surface model $p_{1,GT}$ exhibits normal dynamics, three LVs suffered from a temporal contraction shift on the lateral wall of 10 % ($p_{2,GT}$, $\delta = 0.1$, $\sigma = 0.1$), 20 % ($p_{3,GT}$, $\delta = 0.2$, $\sigma = 0.1$) and 30 % ($p_{4,GT}$, $\delta = 0.3$, $\sigma = 0.1$) relative to the heart cycle, and the last ($p_{5,GT}$, $\sigma = 0.05$) had an induced wall defect on the lateral LV wall, i.e. no movement at the lateral wall. All LV surface meshes and defined parameters are publicly available for download at <https://conrad.stanford.edu/data/heart>. In Figure 3, the phantom meshes for $p_{1,GT}$, $p_{5,GT}$ and p_1 are illustrated for both end-diastolic and end-systolic phases.

The 3-D volumes of the different GT phantoms are plotted in Figure 4. The different contraction shifts as well as the wall motion defect are clearly visible in the curves. A more detailed analysis of the volume curves of the affected segments is given in Table 1. For the affected segments (segments 5, 6, 11, 12 and 16) the mean phase of maximal contraction ϕ_{max} is computed. The phase shift for every phantom is given

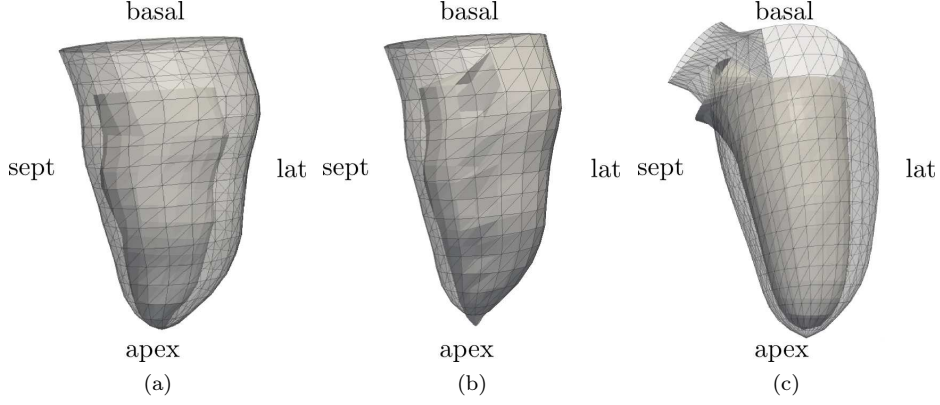


Figure 3: Wall motion of the LV surface models with the wire frame representing the endocardial surface at end-diastole and the solid surface representing the surface mesh at end-systole. (a) Anterior view of the phantom surfaces $p_{1,GT.eps}$ with normal contraction behaviour and in (b) of the phantom surface $p_{5,GT.eps}$ with the lateral wall defect. (c) Anterior view of the estimated surfaces p_1 .

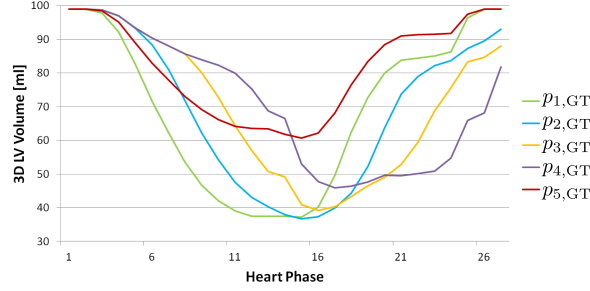


Figure 4: 3-D LV volume curves of the different phantoms ($p_{1,GT}$ – $p_{5,GT}$).

as $\tilde{\delta}$ and the relation to the parameter δ is denoted as ϵ . The motion of the surface points is influenced by the Gaussian function and the flexibility parameter σ . Hence, the maximal phase shift ($\max \tilde{\delta}$) and its relation to the parameter δ is also given in Table 1.

In Table 2, the motion parameters for the different GT phantom datasets are given ($p_{1,GT}$ – $p_{5,GT}$). It can be seen that the normal phantom has an SDI of 4.16 % which is in the upper normal range. In Figure 5a, the Hammer map of $\phi_{i,max}$ of $p_{1,GT}$ is illustrated. It can be seen that the phase to maximal contraction is uniformly distributed over the LV. The $3DFS_i$ Hammer map is given in Figure 6a. On the lateral wall of $p_{1,GT}$, the $3DFS_i$ is ≈ 0.4 . In comparison, $p_{3,GT}$ and $p_{4,GT}$ with the induced lateral phase shift are classified to have a mild or even severe dysfunction with an $SDI \geq 6.0\%$ (Sachpekidis et al. 2011). The phantom $p_{2,GT}$ has a small phase shift and hence only a slightly increased SDI value. In Figure 5b–5d, the Hammer maps of $\phi_{i,max}$ of ($p_{2,GT}$ – $p_{4,GT}$) are illustrated. The increase in the phase to maximal contraction is visible on the lateral wall. The $3DFS_i$ decreases compared to $p_{1,GT}$,

Table 1: Contraction times of affected segments ϕ_{\max} and standard deviation, resulting phase shifts ($\tilde{\delta}$), the relation of $\tilde{\delta}$ to the parameter δ denoted as ϵ . The maximal phase shift ($\max \tilde{\delta}$) is also given for the phantom GT datasets.

Dataset	ϕ_{\max} for affected segments	$\tilde{\delta}$	ϵ to parameter δ	$\max \tilde{\delta}$	ϵ to parameter δ
$p_{1,GT}$	0.52 ± 0.00	-	-	-	-
$p_{2,GT}$	0.60 ± 0.02	0.08	0.02	0.11	0.01
$p_{3,GT}$	0.67 ± 0.03	0.15	0.05	0.18	0.02
$p_{4,GT}$	0.79 ± 0.02	0.27	0.03	0.29	0.01
$p_{5,GT}$	n.a.	n.a.	n.a.	n.a.	n.a.

Table 2: Heart rate (HR), ejection fraction (EF), and the systolic dyssynchrony index (SDI) of the GT phantom datasets.

Dataset	phase shift	HR [bpm]	EF [%]	SDI [%]
$p_{1,GT}$	0 % [lateral]	60	62.37	4.16
$p_{2,GT}$	10 % [lateral]	60	62.97	5.22
$p_{3,GT}$	20 % [lateral]	60	60.40	6.47
$p_{4,GT}$	30 % [lateral]	60	53.65	12.74
$p_{5,GT}$	0 % [defect lateral]	60	38.70	5.05

c.f. Figure 6b–6d. It can be seen that the phase shifts affect the whole ventricle since the time point of the end-diastole and end-systole differs compared to $p_{1,GT}$. From Figure 4, it can be observed that the systolic phase is shifted towards the end of one cardiac cycle, therefore, the “normal/healthy” wall part is measured too early and the “impaired” wall motion is measured too late. For phantom $p_{5,GT}$, the defect on the lateral wall is visible in the Hammer maps at the lateral wall (c.f. Figure 5e and 6e). The $3DFS_i$ drops to ≈ 0.0 at the lateral wall for the wall defect. The small EF of $\approx 39\%$ is additionally an indicator for a wall dysfunction. The SDI shows no abnormal behaviour due to its dependence on averaged volumetric information inside the individual segments. The affected segments still contract slightly and show a contraction $\phi_{s,\max}$. However, the Hammer map of $\phi_{i,\max}$ identifies the wall motion defect.

3.2. Clinical Data

Patient datasets were acquired on two clinical C-arm systems (Universitätsklinikum Erlangen and Thoraxcenter, Erasmus MC). The acquisition protocol is based on the description in Subsection 2.1. Two different protocols were used: the first protocol provided 133 projection images with a size of 960×960 pixels and a pixel resolution of 0.3 mm; the second protocol provided 248 projection images with a size of 480×480 pixels with a pixel resolution of 0.6 mm. Both protocols have a scan time of ~ 5 s. The generated surface models consisted of a different number of heart phases 26.5 ± 6.70 depending on the frames per cardiac cycle and hence the patient’s heart rate. The meshes had 545 control points uniformly distributed over the left ventricle. The examining cardiologists diagnosed no pathological LV dynamics on all eight patient data sets.

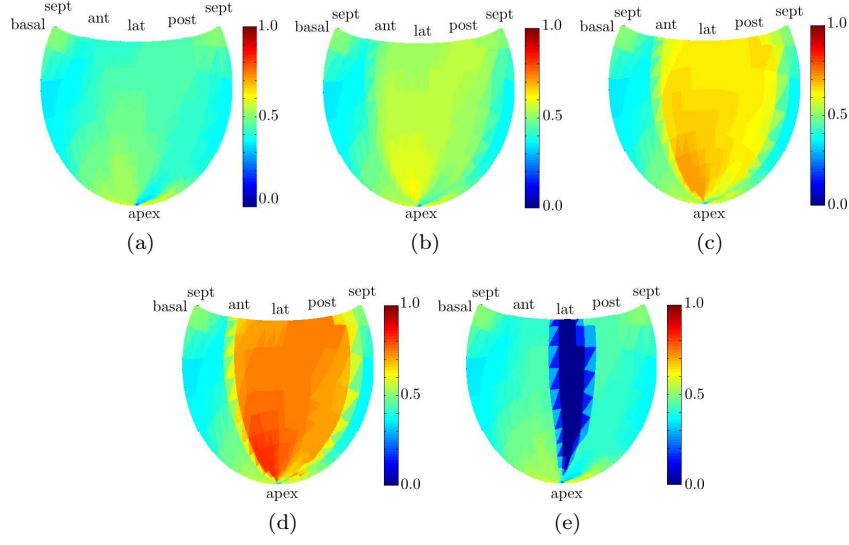


Figure 5: Ground truth Hammer map of $\phi_{i,max}$ of the phantom dataset with (a) normal, synchronous LV contraction ($p_{1,GT}$), (b) relative phase shift of 10% on lateral wall ($p_{2,GT}$) (c) relative phase shift of 20% on lateral wall ($p_{3,GT}$) and (d) relative phase shift of 30% on lateral wall ($p_{4,GT}$) (e) lateral wall defect ($p_{5,GT}$).

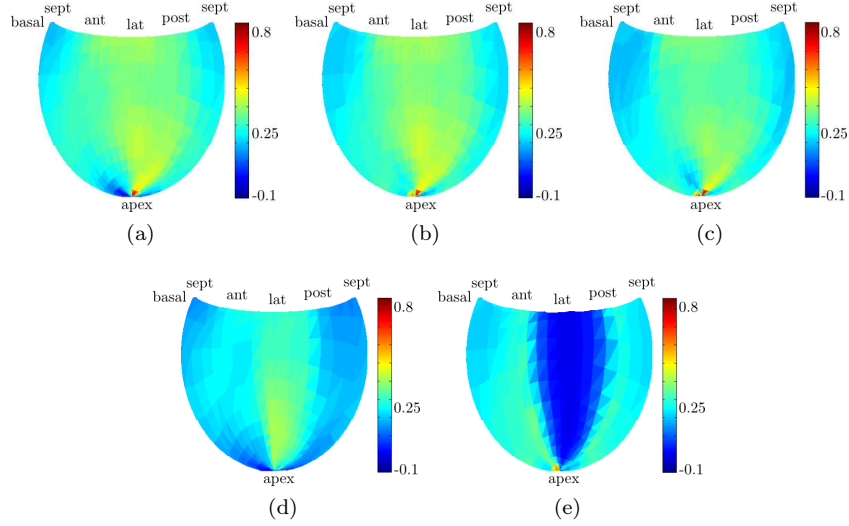


Figure 6: Ground truth Hammer map of $3DFS_i$ of the phantom dataset with (a) normal, synchronous LV contraction ($p_{1,GT}$), (b) relative phase shift of 10% on lateral wall ($p_{2,GT}$) (c) relative phase shift of 20% on lateral wall ($p_{3,GT}$) and (d) relative phase shift of 30% on lateral wall ($p_{4,GT}$) (e) lateral wall defect ($p_{5,GT}$).

Table 3: Mean point-to-mesh error ϵ , the median ($Q_{0.5}$) and the maximal error (max ϵ) for the five different phantom datasets averaged over the mesh points and all time steps with respective standard deviations.

Dataset	ϵ [mm]	$Q_{0.5}$ [mm]	max ϵ [mm]
p_1	1.11 ± 0.18	1.05	1.76
p_2	2.12 ± 1.18	1.72	4.91
p_3	1.25 ± 0.30	1.19	1.99
p_4	1.31 ± 0.29	1.25	2.01
p_5	1.21 ± 0.25	1.12	1.83
	1.40 ± 0.41	1.27 ± 0.26	2.5 ± 1.35

4. Results and Discussion

4.1. Phantom Data

4.1.1. Mesh Error Analysis. In Table 3, an average point-to-mesh error ϵ is used for measuring the difference between the estimated meshes (p_1 – p_5) and the ground truth meshes ($p_{1,GT}$ – $p_{5,GT}$) over all time points. A final point-to-mesh error of 1.40 ± 0.41 mm over all phantom datasets is achieved. It can be seen that the phase shift of 10 % of p_2 results in the highest maximal point-to-mesh error. A reason for this may be that the small deviation in the lateral wall is not visible in a large number of 2-D projection images which are used to build the dynamic model. Overall, when setting the point-to-mesh error in relation to the ventricle size, defined as twice the distance to the long axis, the percentage error is $\approx 3\%$. A small mismatch between the estimated mesh p_1 and the ground truth $p_{1,GT}$ is due to the smoother appearance and the different mesh topology of the generated meshes (c.f. Figure 3).

4.1.2. Heart Phase Identification Analysis. In order to evaluate the accuracy of the heart phase identification, the five phantom datasets are used. In Table 4, the error between the ground truth heart phase and the estimated heart phases of p_1 – p_5 is given. For the phantom experiments a number of $K = 27$ bins was chosen. The mean error is denoted with ϵ_ϕ given in relative heart phases between $[0, 1]$. The overall mean error ϵ_ϕ of all phantom datasets is 0.06 ± 0.02 . Furthermore, the mean error ϵ_{ϕ_k} of the binned heart phase is also given. The overall mean ϵ_{ϕ_k} is less than one heart phase bin and results in 0.78 ± 0.28 . A scatter plot of the ground truth heart phase number and the estimated heart phase is illustrated in Figure 7a. A small number of outliers can be seen of maximum 2 bins at diastolic heart phases. The small mismatch may be due to the longer lasting diastole where the 3-D volume is almost constant and hence the detection of the ED phase can vary slightly.

In order to evaluate if the bloodpool size variation due to cardiac phase variation can be distinguished from perspective size variations due to the rotation of the C-arm, a correlation coefficient ρ_π between the original segmented 2-D bloodpool signal $\pi(t)$ and the 3-D volume signal $\Pi(t)$ is computed. The mean correlation ρ_π for all five phantom datasets is 0.74 ± 0.07 . However, in order to identify the respective heart phase, the bloodpool signal is normalized as described in Section 2.4. Therefore, the correlation coefficient ρ_{π_n} is also given for the normalized bloodpool signal $\pi_n(t)$ and the 3-D volume signal $\Pi(t)$. Here, the mean correlation coefficient results in 0.98 ± 0.02 for p_1 – p_5 . Thus, the change in the bloodpool size due to the cardiac phase can

Table 4: Accuracy and correlation of the heart phase identification for the phantom datasets. The mean relative heart phase error ϵ_ϕ and the mean error of the binned heart phase ϵ_{ϕ_k} and their standard deviations are given. The correlation coefficients between the original segmented 2-D bloodpool signal $\pi(t)$ and the 3-D volume $\Pi(t)$ are given as ϱ_π . And the correlation coefficient between the normalized 2-D bloodpool signal $\pi_n(t)$ and $\Pi(t)$ is given as ϱ_{π_n} .

Dataset	K	ϵ_ϕ [%]	ϵ_{ϕ_k} [bins]	ϱ_π	ϱ_{π_n}
p_1	27	0.06 ± 0.16	0.60 ± 0.59	0.82	0.99
p_2	27	0.05 ± 0.14	0.51 ± 0.60	0.80	0.99
p_3	27	0.04 ± 0.14	0.74 ± 0.79	0.74	0.98
p_4	27	0.07 ± 0.16	1.24 ± 1.26	0.67	0.94
p_5	27	0.08 ± 0.18	0.80 ± 0.78	0.69	0.99
	27	0.06 ± 0.02	0.78 ± 0.28	0.74 ± 0.07	0.98 ± 0.02

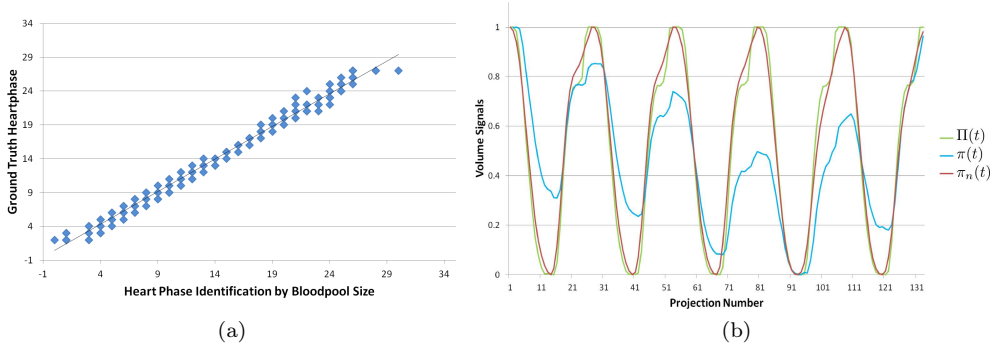


Figure 7: (a) Correlation between heart phases identified by 2-D bloodpool size and the ground truth heart phase of phantom p_1 . (b) 3-D volume signal $\Pi(t)$, the 2-D segmented bloodpool signal $\pi(t)$ and the normalized bloodpool signal $\pi_n(t)$ of phantom dataset p_1 .

be distinguished from the perspective size variations due to the normalization step. The bloodpool signal $\pi(t)$, the normalized bloodpool $\pi_n(t)$ and the 3-D volume signal $\Pi(t)$ of phantom p_1 are illustrated in Figure 7b.

4.1.3. Motion Analysis. In Table 5, the quantitative results for the estimated phase shifts of (p_1-p_5) are given. The deviation between (p_1-p_5) and $(p_{1,GT}-p_{5,GT})$ is stated in column three. The overall deviation of the mean phase shift is $\approx 9\%$ of a cardiac cycle and for the maximal phase shift $\approx 7\%$ of a cardiac cycle.

The results for the motion analysis parameter for the phantom meshes compared to the GT meshes are given in Table 6. In general it can be seen that the estimated meshes underestimate the EF and the SDI values in most datasets. However, the tendency between the estimated and the ground truth values are similar and show the same noticeable pathologies as the GT values. In Figure 8, the Hammer maps with $\phi_{i,\max}$ for p_1-p_5 are shown. For dataset p_1 , the Hammer map (Figure 8a) shows a homogeneous distribution as in the GT map of $p_{1,GT}$ in Figure 5a. For p_2-p_4 , the increase of the motion deficit is visible on the lateral wall. For p_2 and p_3 a smaller

Table 5: Contraction times of affected segments ϕ_{\max} , the error compared to the GT ϕ_{\max} given in Table 1 and the error between the maximal phase shifts ($\max \tilde{\delta}$) and standard deviations.

Dataset	ϕ_{\max} for affected segments	ϕ_{\max} error to GT	$\max \tilde{\delta}$ error to GT
p_1	0.45 ± 0.03	0.07	0.02
p_2	0.48 ± 0.03	0.12	0.13
p_3	0.58 ± 0.03	0.09	0.08
p_4	0.70 ± 0.05	0.09	0.04
p_5	n.a.	n.a.	n.a.
		0.09 ± 0.02	0.07 ± 0.05

Table 6: Ejection fraction (EF), systolic dyssynchrony index (SDI) of the phantom datasets and the deviation σ to the ground truth phantom datasets and the standard deviation.

Dataset	EF [%]	σ to GT	SDI [%]	σ to GT
p_1	62.39	0.02	3.68	-0.61
p_2	59.63	-3.34	3.50	-1.72
p_3	54.11	-6.29	5.08	-1.39
p_4	49.16	-4.49	9.42	-3.32
p_5	41.49	2.79	6.16	1.11
		3.39 ± 2.31		1.60 ± 1.03

band on the lateral wall is delayed compared to the GT LV meshes. The phantom p_3 with 30% phase shift in Figure 8d shows a high correlation with the GT Hammer map in Figure 5d. For the phantom with the lateral wall defect, a reduction of the motionless band can be identified. A small overshoot is visible close to the lateral wall (Figure 5e and Figure 8e). The small deviation of the GT meshes and the estimated meshes are given in the difference $\phi_{i,\max}$ Hammer maps in Figure 9. For p_5 the slight overshoots at the lateral wall are visible. The 3DFS_i Hammer maps are illustrated in Figure 10. In Figure 11, the corresponding difference maps are given. They show that the highest deviation between the meshes occurs around the apex region.

4.2. Clinical Data

4.2.1. Motion Analysis. The results for the eight patient datasets are given in Table 7 (d_1 – d_8). It can be observed that all patients are classified as healthy using the SDI according to (Kapetanakis et al. 2005, Sachpekidis et al. 2011). An example of the surface meshes of dataset d_2 is shown in Figure 12a and the dynamic contraction curves for each segment’s subvolume for dataset d_2 are shown in Figure 12b. All segments contract synchronously, hence the curves have almost the same $\phi_{s,\max}$ and a small SDI. In Figure 13a, $\phi_{i,\max}$ of dataset d_2 is shown. The maximal contraction phase is homogeneously distributed over the whole LV. Small hypokinetic regions are indicated by mesh points close to the apex point, as visible in the 3DFS_i Hammer map of dataset d_2 in Figure 13b, as well as on the 3-D overlay in Figure 13c. The motion close to the apex is small compared to the remaining mesh, hence this area is

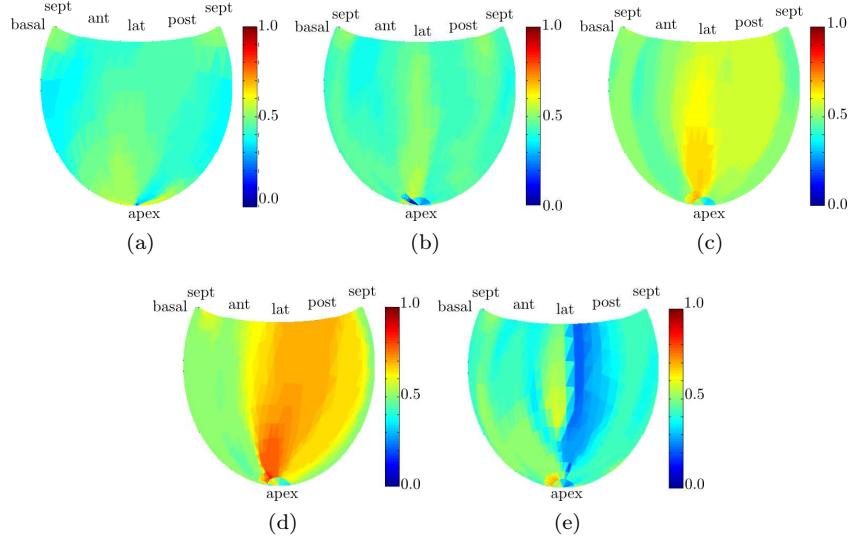


Figure 8: Estimated Hammer map of $\phi_{i,\max}$ of the phantom dataset with (a) normal, synchronous LV contraction (p_1), (b) relative phase shift of 10 % on lateral wall (p_2) (c) relative phase shift of 20 % on lateral wall (p_3) and (d) relative phase shift of 30 % on lateral wall (p_4) (e) lateral wall defect (p_5).

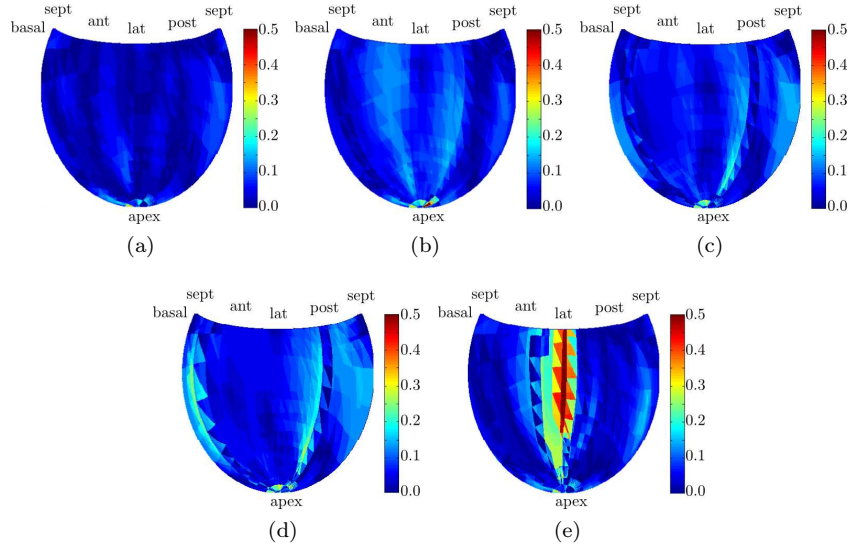


Figure 9: Difference Hammer map of $\phi_{i,\max}$ of the ground truth and the estimated phantom dataset with (a) normal, synchronous LV contraction ($|p_1-p_{1,GT}|$), (b) relative phase shift of 10 % on lateral wall ($|p_2-p_{2,GT}|$) (c) relative phase shift of 20 % on lateral wall ($|p_3-p_{3,GT}|$) and (d) relative phase shift of 30 % on lateral wall ($|p_4-p_{4,GT}|$) (e) lateral wall defect ($|p_5-p_{5,GT}|$).

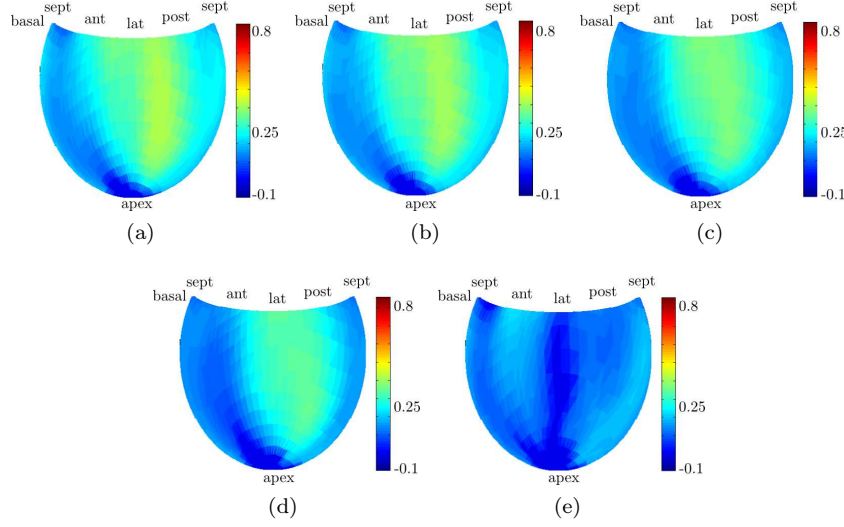


Figure 10: Estimated Hammer map of $3DFS_i$ of the phantom dataset with (a) normal, synchronous LV contraction (p_1), (b) relative phase shift of 10 % on lateral wall (p_2) (c) relative phase shift of 20 % on lateral wall (p_3) and (d) relative phase shift of 30 % on lateral wall (p_4) (e) lateral wall defect (p_5).

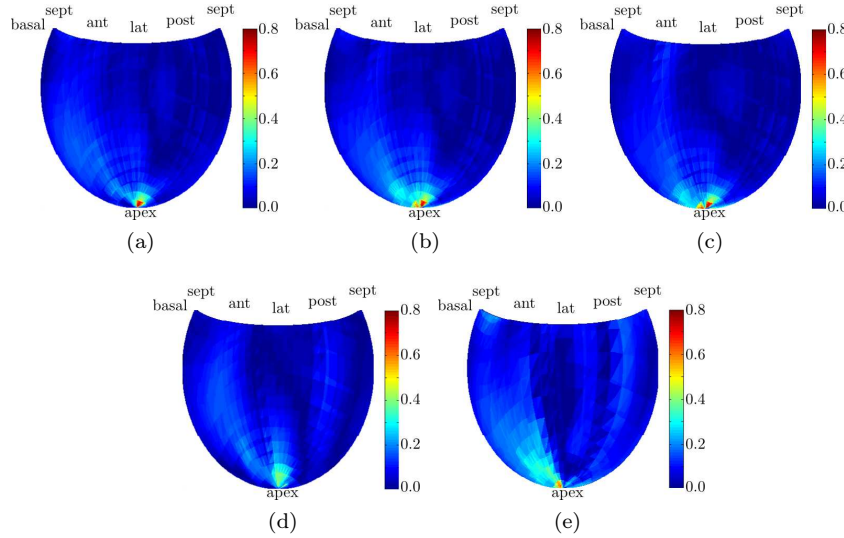


Figure 11: Difference Hammer map of $3DFS_i$ of the ground truth and the estimated phantom dataset with (a) normal, synchronous LV contraction ($|p_1-p_{1,GT}|$), (b) relative phase shift of 10 % on lateral wall ($|p_2-p_{2,GT}|$) (c) relative phase shift of 20 % on lateral wall ($|p_3-p_{3,GT}|$) and (d) relative phase shift of 30 % on lateral wall ($|p_4-p_{4,GT}|$) (e) lateral wall defect ($|p_5-p_{5,GT}|$).

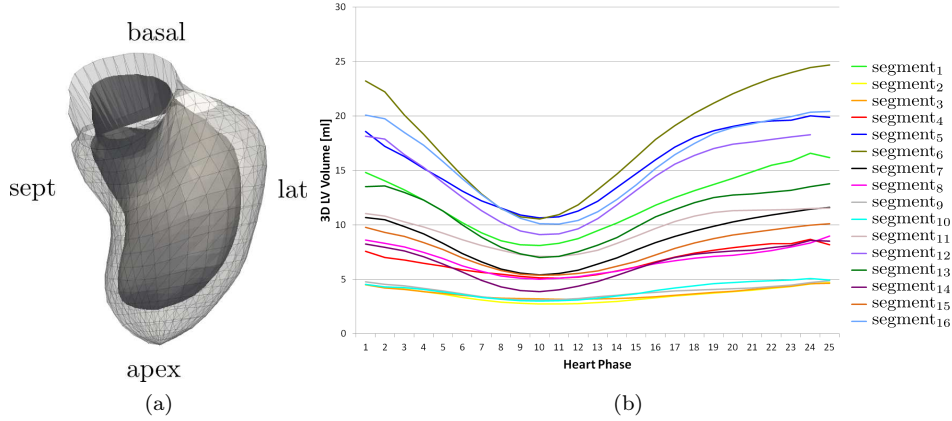


Figure 12: (a) Anterior view of the estimated LV surface meshes of d_2 with the wire frame representing the endocardial surface at end-diastole and the solid surface representing the surface mesh at end-systole. (b) 3-D LV volume curves for each segment of dataset d_2 over the different heart phases.

Table 7: Heart rate (HR), ejection fraction (EF), and the systolic dyssynchrony index (SDI) of the clinical patient datasets.

Dataset	HR [bpm]	EF [%]	SDI [%]
d_1	73.4 ± 8.4	63.08	1.22
d_2	63.9 ± 0.8	50.32	1.79
d_3	52.7 ± 0.5	56.69	1.79
d_4	62.9 ± 2.9	58.73	2.88
d_5	55.3 ± 9.3	62.33	3.42
d_6	59.9 ± 0.4	72.26	2.08
d_7	58.3 ± 0.3	50.98	2.85
d_8	88.6 ± 25.6	70.58	2.48

sensitive to errors introduced by the 2-D segmentation, position of the points to the principal axis \mathbf{n}_1 and the consistency of data from different heart cycles.

4.2.2. Principle Axis Alignment. The PCA does not necessarily yield an axis \mathbf{n}_1 which passes through the apex, since the LV is not necessarily symmetric. For that reason the local coordinate system is rotated in order to align \mathbf{n}_1 with the long axis given by the mid point of the mitral valve and the apex. These points are detected by the initial model-based surface mesh fitting on the non-gated C-arm CT volume (Zheng et al. 2008). During deformation of the initial mesh to fit the 2-D angiographic data, the topology of the 3-D mesh is preserved, and the apex and mitral valve points

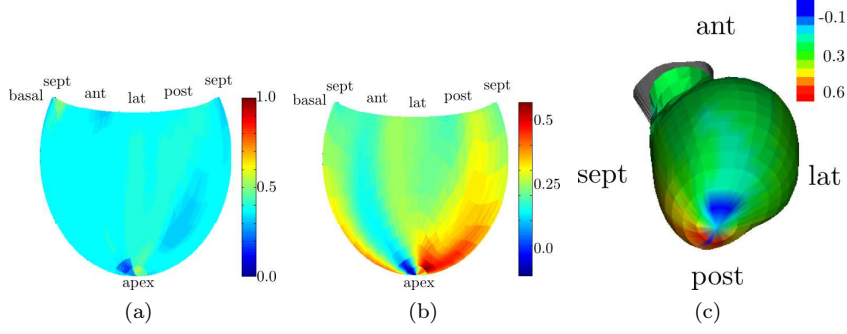


Figure 13: Hammer map of (a) $\phi_{i,\max}$ of dataset d_2 , (b) $3DFS_i$ of dataset d_2 , (c) Colour overlay of the $3DFS_i$ onto the endocardial LV surface of dataset d_2 .

Table 8: Rotation angle variation of the clinical datasets.

Dataset	d_1	d_2	d_3	d_4	d_5	d_6	d_7	d_8	$\overline{\angle_{\text{rot}}}$
\angle_{rot}	9.14	7.46	6.33	8.37	14.86	17.92	16.54	16.36	12.12 ± 4.73

(mitral valve annulus) are consistent over the whole cardiac cycle. The rotation of the axis \mathbf{n}_1 to the long axis with the rotation angle \angle_{rot} can be performed accurately. In Table 8, the rotation angles for the clinical datasets are given.

4.3. Limitations and Challenges

Spatial resolution is limited by the number of projection images used for the dynamic mesh fitting process. Here, the scan time was 5 s, resulting in total 5 projections per heart phase with a heart rate of 60 bpm. By increasing the scan time to 8 s, a total of 8 projection images might be used to regularize the dynamic LV mesh generation and hence to increase the spatial resolution, but a longer scan time implies a higher radiation dose and a higher contrast burden for the patient.

As previously mentioned, the motion close to the apex is small compared to the remaining mesh, hence this area is sensitive to errors introduced by the 2-D segmentation. In general, 2-D segmentation errors occur since the original LV surface is quite structured due to the papillary muscles. However, a smooth boundary is extracted from the 2-D projections for the surface mesh generation. It is known that during the surface generation, the assumption of motion along the surface-normal is reasonable for the middle and basal LV segments, but not good for the LV apex, since many intersections in the trajectories of mesh points around the apex can occur. In a first clinical prototype, the motion in the apex could be greyed out for the visualization in order to avoid misleading the cardiologist. In the future, the issue can be mitigated by using a learned prior mean motion trajectory from dynamic cardiac CT sequences (Chen et al. 2013). Up to now, the evaluation of the presented wall motion analysis framework is a feasibility study. The next step in the evaluation of the framework is a validation of the extracted parameters compared to parameters estimated from MRI or 3-D echocardiography.

5. Conclusion and Outlook

In this paper, we presented the first framework which enables LV wall motion analysis directly in the catheter lab during a cardiac intervention using intra-procedural C-arm CT data. The feasibility study on simulated phantom LVs as well as on eight clinical datasets indicate the capability of the presented framework. The simulation study showed promising qualitative and quantitative preliminary results. The limited spatial sampling due to the short scan time induces errors in the surface model. However, the induced pathologies could all be identified by the wall motion parameters used here. The dynamic surface model together with the colour overlay in 3-D may provide additional value. Currently, the apex region should be greyed out since errors are amplified in this region. Improvements regarding these issues are works in progress. At the time of submission, no clinical cases with LV dyssynchrony were available for evaluation, but a clinical study has been initiated. As a future step, the created LV model together with the wall analysis can be overlayed onto 2-D fluoroscopic images for guidance to the cardiologist.

Disclaimer: The concepts and information presented in this paper are based on research and are not commercially available.

Acknowledgments

The authors thank Dr. Rittger, Universitätsklinikum Erlangen, Germany and Dr. Schultz, Thoraxcenter, Erasmus MC, Rotterdam, Netherlands for providing the clinical data. The authors also gratefully acknowledge funding support from the NIH grant R01 HL087917 and of the Erlangen Graduate School in Advanced Optical Technologies (SAOT) by the German Research Foundation (DFG) in the framework of the German excellence initiative.

References

- Backfrieder W, Carpella M, Swoboda R, Steinwender C, Gabriel C & Leisch F 2005 Model based LV-reconstruction in bi-plane X-ray angiography *in* J Fitzpatrick & J Reinhardt, eds, 'Proceedings of SPIE Medical Imaging 2005' Vol. 5747 pp. 1475–1483.
- Cerqueira M D, Weissman N J, Dilsizian V, Jacobs A K, Kaul S, Laskey W K & et al 2002 Standardized myocardial segmentation and nomenclature for tomographic imaging of the heart *Circulation* **105**(4), 539–542.
- Chen M, Zheng Y, Müller K, Rohkohl C, Lauritsch G, Boese J, Funka-Lea G, Hornegger J & Comaniciu D 2011 Automatic extraction of 3D dynamic left ventricle model from 2D rotational angiocardiogram *in* G Fichtinger, A Martel & T Peters, eds, 'Proceedings of the Medical Imaging and Computer Assisted Interventions (MICCAI) 2011' Vol. 6893 of *Lecture Notes in Computer Science* Springer Verlag Berlin Heidelberg pp. 471–478.
- Chen M, Zheng Y, Wang Y, Müller K & Lauritsch G 2013 Automatic 3D motion estimation of left ventricle from c-arm rotational angiocardiography using a prior motion model and learning based boundary detector *in* K Mori, I Sakuma, Y Sato, C Barillot & N Navab, eds, 'Proceedings of the Medical Imaging and Computer Assisted Interventions (MICCAI) 2013' Vol. 8151 of *Lecture Notes in Computer Science* Springer Verlag Berlin Heidelberg pp. 90–97.
- Feldkamp L, Davis L & Kress J 1984 Practical cone-beam algorithm *J Opt Soc Am A* **1**(6), 612–619.
- Gimenes V, Vieira M, Andrade M, Pinheiro Jr J, Hotta V & Mathias Jr W 2008 Standard values for real-time transthoracic three-dimensional echocardiographic dyssynchrony indexes in a normal population *J Am Soc Echocardiogr* **21**(11), 1229–1235.
- Hartley R I & Zisserman A 2004 *Multiple View Geometry in Computer Vision* 2nd edn Cambridge University Press.
- Herz S, Ingrassia C, Homma S, Costa K & Holmes J 2005 Parameterization of left ventricular wall motion for detection of regional ischemia *Ann Biomed Eng* **33**(7), 912–919.

- Hunter P & Smaill B 1988 The analysis of cardiac function: A continuum approach *Prog Biophys Mol Bio* **52**(2), 101–164.
- Isola A, Grass M & Niessen W 2010 Fully automatic nonrigid registration-based local motion estimation for motion-corrected iterative cardiac CT reconstruction *Med Phys* **37**(3), 1093–1109.
- Jenkins C, Bricknell K, Hanekom L & Marwick T 2004 Reproducibility and accuracy of echocardiographic measurements of left ventricular parameters using real-time three-dimensional echocardiography *J Am Coll Cardiol* **44**(4), 8788–886.
- Kapetanakis S, Kearney M, Siva A, Gall N, Cooklin M & Monaghan M 2005 Real-time three-dimensional echocardiography a novel technique to quantify global left ventricular mechanical dyssynchrony *Circulation* **112**(7), 992–1000.
- Lauritsch G, Boese J, Wigström L, Kemeth H & Fahrig R 2006 Towards cardiac C-arm computed tomography *IEEE Trans Med Imaging* **25**(7), 922–934.
- Lee H, Kim S, Hanna E & Schoepf U 2012 Impact of ventricular contrast medium attenuation on the accuracy of left and right ventricular function analysis at cardiac multi detector-row CT compared with cardiac MRI. *Acad Radiol* **19**(4), 395–405.
- Ma Y L, Shetty A, Duckett S, Etyngier P, Gijssbers G, Bullens R, Schaeffter T, Razavi R, Rinaldi C & Rhode K 2012 An integrated platform for image-guided cardiac resynchronization therapy *Phys Med Biol* **57**(10), 2953–2968.
- Maier A, Hofmann H, Berger M, Fischer P, Schwemmer C, Wu H, Müller K, Hornegger J, Choi J H, Riess C, Keil A & Fahrig R 2013 Conrad - a software framework for cone-beam imaging in radiology *Med Phys* **40**(11), 111914–1–8.
- Maier A, Hofmann H, Schwemmer C, Hornegger J, Keil A & Fahrig R 2012 Fast simulation of X-ray projections of spline-based surfaces using an append buffer *Phys Med Biol* **57**(19), 6193–6210.
- Mantilla J, Bravo A & Medina R 2008 A 3-D multi-modality image framework for left ventricle motion analysis in ‘International Machine Vision and Image Processing Conference (IMVIP)’ pp. 130–135.
- Matthew S, Gandy S J, Nicholas R S, Waugh S A, Crowe E A, Lerski R A, Dunn M H & Houston J G 2012 Quantitative analysis of cardiac left ventricular variables obtained by MRI at 3 T: a pre- and post-contrast comparison. *Brit J Radiol* **85**(1015), 343–347.
- Medina R, Garreau M, Toro J, Breton H, Coatrieux J L & Jugo D 2006 Markov random field model for three-dimensional reconstruction of the left ventricle in cardiac angiography *IEEE Trans Med Imaging* **25**(8), 1087–1100.
- Müller K, Maier A, Fischer P, Bier B, Lauritsch G, Schwemmer C, Fahrig R & Hornegger J 2013 Left ventricular heart phantom for wall motion analysis in ‘IEEE Proceedings of the NSS/MIC 2013’.
- Müller K, Zheng Y, Wang Y, Lauritsch G, Rohkohl C, Schwemmer C, Maier A, Schultz C, Hornegger J & Fahrig R 2013 Evaluation of interpolation methods for surface-based motion compensated tomographic reconstruction for cardiac angiographic C-arm data *Med Phys* **40**(3), 031107–1–12.
- Moriyama M, Sato Y, Naito H, Hanayama M, Ueguchi T, Harada T, Yoshimoto F & Tamura S 2002 Reconstruction of time-varying 3-D left-ventricular shape from multiview X-Ray cineangiograms *IEEE Trans Med Imaging* **21**(7), 773–785.
- Moynihan P, Parisi A & Feldman C 1981 Quantitative detection of regional left ventricular contraction abnormalities by two-dimensional echocardiography. I. Analysis of methods. *Circulation* **63**(4), 752–760.
- Pfisterer M, Battler A & Zaret B 1985 Range of normal values for left and right ventricular ejection fraction at rest and during exercise assessed by radionuclide angiography *Eur Heart J* **6**(8), 647–655.
- Po M, Srichai M & Laine A 2011 Quantitative detection of left ventricular dyssynchrony from cardiac computed tomography angiography in ‘Proceedings of the 8th IEEE International Symposium on Biomedical Imaging: From Nano to Macro (ISBI 2011)’ pp. 1318–1321.
- Prümmer M, Hornegger J, Lauritsch G, Wigström L, Girard-Hughes E & Fahrig R 2009 Cardiac C-Arm CT: A unified framework for motion estimation and dynamic CT *IEEE Trans Med Imaging* **28**(11), 1836–1849.
- Sachpekidis V, Bhan A & Monaghan M J 2011 xii edn Springer Verlag London Limited chapter 7, pp. 64–67.
- Segars W, Lalush D & Tsui B 1999 A realistic spline-based dynamic heart phantom *IEEE Trans Nucl Science* **46**(3), 503–506.
- Segars W, Mahesh M, Beck T, Frey E & Tsui B 2008 Realistic CT simulation using the 4D XCAT phantom *Med Phys* **35**(8), 3800–3808.

- Swoboda R, Carpella M, Steinwender C, Gabriel C, Leisch F & Backfrieder W 2005 From 2D to 4D in quantitative left ventricle wall motion analysis of biplanar x-ray angiograms *in* 'Computers in Cardiology' Vol. 32 pp. 977–980.
- Tu Z 2005 Probabilistic boosting-tree: learning discriminative models for classification, recognition, and clustering *in* 'Tenth IEEE International Conference on Computer Vision, 2005 (ICCV 2005)' Vol. 2 pp. 1589–1596.
- Zheng Y, Barbu A, Georgescu B, Scheuering M & Comaniciu D 2008 Four-chamber heart modeling and automatic segmentation for 3D cardiac CT volumes using marginal space learning and steerable features *IEEE Trans Med Imaging* **27**(11), 1668–1681.